

# Ultra-Flexible Biodegradable Pressure Sensitive Field Effect Transistors for Hands-Free Control of Robot Movements

Ambarish Paul, Nivasan Yogeswaran, and Ravinder Dahiya\*

Sensitive flexible pressure sensors are needed in applications such as health monitoring, robotics, and wearable systems. Herein, crumpled graphene flakes network (c-GFN) channel based highly sensitive pressure sensing field effect transistors (PRESSFETs) are presented. The solution-processed PRESSFET devices are developed on ultrathin ( $\approx 3 \mu\text{m}$  thick) biodegradable graphene oxide–chitosan (GO–CS) substrate. The distinctive crumpled morphology of GFN leads to a bandgap of 800 meV, which allows the device to have clear ON and OFF electronic states and low subthreshold swing. The presented device can work over a dynamic pressure range (0.5–2 kPa), while exhibiting good electrical stability and repeatability during rapid switching. The application of the presented device is demonstrated by attaching them to the temple regions of the face and pressing them with flexure and relaxation of respective temporalis muscles for hands-free control of the movements of a robotic device. The pressure sensing device turns ON when the facial temporalis muscle is flexed and returns to the OFF state when it is relaxed. Finally, the degradability of the devices is presented to demonstrate their easy disposability and potential for zero electronic waste.

## 1. Introduction

Flexible pressure sensors are needed in numerous application areas such as biomedical, robotics, sports, gaming, and rehabilitation.<sup>[1–5]</sup> In these applications, they either provide a measure of physiological parameters such as blood pressure<sup>[6]</sup> or the haptic feedback to control movements of robotic limbs, or the touch-based communication via wearable smart gloves<sup>[7,8]</sup> They could also allow controlled movements of assistive tools used by paralytic patients and amputees, for example, by capturing the muscle movements through electromyography (EMG). In such cases, the pressure sensors need to be highly sensitive as

A. Paul, N. Yogeswaran, R. Dahiya  
Bendable Electronics and Sensing Technologies (BEST) Group  
James Watt School of Engineering  
University of Glasgow  
Glasgow G12 8QQ, UK  
E-mail: Ravinder.Dahiya@glasgow.ac.uk

The ORCID identification number(s) for the author(s) of this article can be found under <https://doi.org/10.1002/aisy.202200183>.

© 2022 The Authors. Advanced Intelligent Systems published by Wiley-VCH GmbH. This is an open access article under the terms of the Creative Commons Attribution License, which permits use, distribution and reproduction in any medium, provided the original work is properly cited.

DOI: 10.1002/aisy.202200183

the EMG signals from muscles are often feeble ( $\approx$  few  $\mu\text{V}$  to 1 mV). Further, the pressure sensor with switching capability is needed for better control. Herein, we present such a device which combines sensitive pressure sensing with transistor switching operation to control robotic movements.

The graphene-based field effect transistor (FET) devices presented here utilized the solution-processed graphene flakes network (GFN) as the channel, Ecoflex as the dielectric material, and graphene oxide (GO)–chitosan (CS) as the substrate. Different forms of graphene (e.g., monolayered graphene, graphene nanoribbons, bilayer graphene, graphene ink with suspended nanoflakes, solution-processed graphene flakes, etc.) were explored in past as the active channel material in FET devices. However, the fabrication process for such devices was complex. For example, the monolayer and bilayer graphene transfer

techniques suffer from issues such as contamination during wet transfer, complicated voltage optimization during electrochemical bubble transfer technique, and crack formation during dry and roll-to-roll transfer.<sup>[9–11]</sup> Further, the traces of etchant residue during support-free transfer reduces their performance, and the transfer of hydrophobic graphene on a hydrophilic substrate such as CS was difficult. In contrast, the solution-processed routes for deposition of graphene flakes, to develop the GFN, were much simple, cost-effective, and suitable for flexible substrates. However, due to the low ON/OFF ratio (generally  $< 2$ ), the devices with GFN as the channel material could not yield high performance, which is a major bottleneck for their use in switching applications. As a result, their application was restricted to the FET-based sensors.<sup>[12–15]</sup> This could be addressed through the utilization of nanostructured crumpled GFN as the channel material.<sup>[16]</sup> The nanocorrugations in GFN morphology produce a bandgap (800 meV) opening in its electronic structure. The nanocorrugations on the GO–CS, achieved by mutual electrostatic steric repulsion of neighboring CS-grafted GO microflakes can be controlled by the concentration of GO in GO–CS. This method of obtaining crumpled morphology is easier than other physical techniques<sup>[17]</sup> and can also be used for a large area.

The crumpled graphene flakes network (c-GFN) based pressure sensing field effect transistor (PRESSFET) was designed to operate as a wearable switching device for the hands-free control of the robotic platform. The device exploited the temporalis

muscle of the temple region of the face to trigger the switching operation in PRESSFET. Pressure-sensitive FETs on the flexible substrate were reported earlier for touch sensing in robotics, fitness tracking, fingerprint sensors, blood pressure, and wound healing monitoring,<sup>[2,18–23]</sup> their use as wearable electronic switches has not been reported yet. The bandgap of 800 meV in c-GFN morphology helped to achieve distinct ON and OFF switching states in the pressure sensing range of 500–2500 Pa and allowed the use of PRESSFETs as a control device. With the union of sensor and transistor functions, the PRESSFET device could also offer signal amplification, better signal-to-noise ratio, and simply the sensor frontend electronic circuitry.<sup>[4,24,25]</sup> Considering the on-skin wearable device application, the PRESSFETs have been fabricated on biodegradable GO–CS substrate. The use of GO–CS as biocompatible and biodegradable material in wearable devices could also facilitate easy disposability.<sup>[4,19,24,26–30]</sup>

## 2. Device Design

The ultra-thin, highly sensitive flexible PRESSFETs were developed on biodegradable GO cross-linked chitosan (GO–CS) substrate. The device architecture is schematically shown in **Figure 1a**. The top-gated FET device comprises solution-processed c-GFN as the channel material (channel length,  $L = 30 \mu\text{m}$ ), biocompatible soft elastomer (i.e., Ecoflex) as the dielectric (700 nm thick), and ultrathin ( $3 \mu\text{m}$  thick) GO–CS as the substrate. Solution-processed network of graphene flakes conformed to the nanocorrugated morphology of the GO–CS substrate to form the c-GFN as depicted in **Figure 1(inset)**. The ultrathin substrate of the device was illustrated by wrapping it on a polymer swab as shown in **Figure 1b**. The thickness of the GO–CS substrate was measured using Dektak Profilometer 3D

through line scan profile from point A to point B and was found to be  $3 \mu\text{m}$  as shown in **Figure 1c–i,c-ii**, respectively. The crumpled (c-) morphology with nanostructured wrinkles of GFN in the channel enables the transformation of the electronic structure of graphene flakes network from  $sp^2$  hybridized state to  $sp^2$ – $sp^3$  state, thereby opening a narrow bandgap of 800 meV, required for transistor operation<sup>[31,32]</sup> (See Section S1 and S2, Supporting Information). Although a few layers of planar graphene show a natural semimetallic behavior, its transformation to crumpled morphology in GFN imparts semiconducting property to the FET channel. The c-GFN as the channel material facilitates achieving an enhanced ON/OFF ratio ( $\approx 15$ ) and lower subthreshold swing  $S_{\text{subthres}}$  as compared to the devices using planar ( $p$ -) GFN as discussed in Section 4.3.2.

Due to the use of soft material as dielectric, the output current  $I_D$  of PRESSFETs was modulated by the application of external pressure on the gate area. Owing to the low Young's modulus ( $Y = 0.1694 \text{ MPa}$ ), the Ecoflex-based dielectric layer experienced large variation in the thickness at even small external pressure.<sup>[33]</sup> This variation in dielectric thickness in response to external pressure changed the drain current  $I_D$  of the PRESSFET when operated at the ON state. As a result, the presented PRESSFETs were sensitive and offered a much lower detection limit (LDL). The nanocorrugations on the surface of the GO–CS substrate facilitated the formation of the c-GFN channel with nanostructured features. Moreover GO–CS being biodegradable can be easily disposed of in soil and water. The GO-linking in the GO–CS substrate provided mechanical stability to the device<sup>[34]</sup> in an aqueous solution. Further, GO is biocompatible and biodegradable and its enzymatic oxidation could help in the bioremediation.<sup>[35–40]</sup> The GFN in the device can be decomposed by bacteria, fungi, and other enzymatic reactions.<sup>[41]</sup> Graphite is known to be oxidized by microorganisms like the

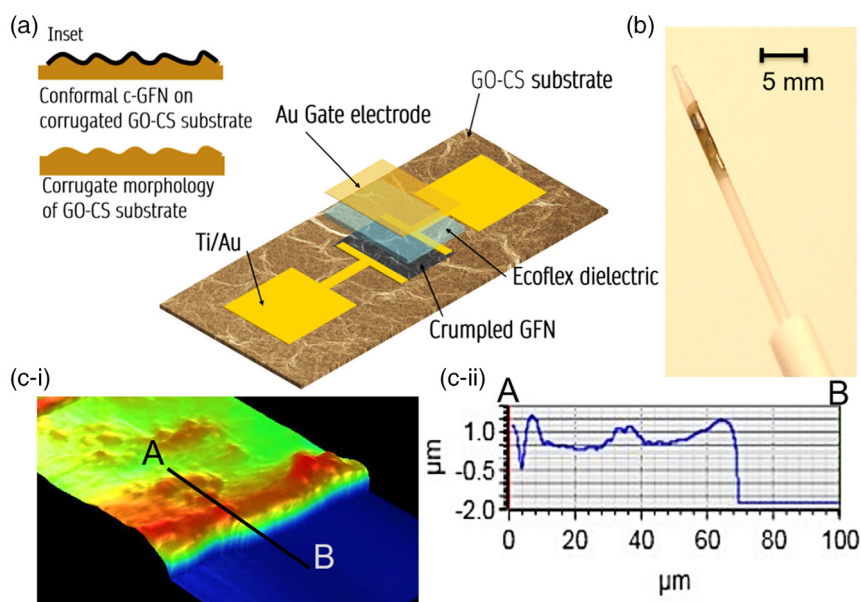


**Figure 1.** a) Schematic representation of pressure sensing field effect transistor (PRESSFET) with top gated architecture and corrugated morphology of graphene oxide–chitosan (GO–CS) substrate facilitating the (inset) formation of corrugated graphene flake network (c-GFN). b) PRESSFET wrapped around a swab (outer diameter  $500 \mu\text{m}$ ). c) Dektak profilometer: i) 3D scan and ii) line scan showing  $\approx 3 \mu\text{m}$  thickness of the GO–CS.

*Acidithiobacillus ferrooxidans* CFMI-1 bacteria to form GO, which can be further decomposed to various by-products with the evolution of carbon dioxide gas.<sup>[42]</sup> Some species of bacteria called the naphthalene-degrading bacteria, commonly found in soil rhizosphere, surface water, and groundwater can also decompose graphene and GO.<sup>[43]</sup> Likewise, Ecoflex can degrade (in about six months) without leaving any residue.<sup>[44,45]</sup> The metallic Au used here as electrodes is not biodegradable, but being a noble metal it has no hazardous effect on microorganisms. Further, Au can be bio-reduced by the fungus *Pycnoporus sanguineus*<sup>[46]</sup> and can even be bio-recovered<sup>[47]</sup> from the same. Au could also be replaced with other degradable conductive materials such as Mg and PEDOT:PSS. The fabrication of presented devices with biodegradable materials is attractive for disposable electronics, which could also help address the rapidly growing challenges related to medical and electronic waste.<sup>[48–50]</sup>

### 3. Materials and Fabrication

CS powder (high molecular weight (MW)) was obtained from Sigma-Aldrich co., 3050, Spruce, USA, and GO was obtained from Graphene Laboratories Inc. NY, USA. The graphene ink and the Ecoflex were purchased from Sigma Aldrich and Amazon respectively. Deionized (DI) water used in the experiments was obtained from the Millipore water filtration system. All the chemicals were analytical-grade reagents.

#### 3.1. Preparation of CS and GO–CS Solutions

A wide range of biocompatible polymers (e.g., polyvinyl chloride (PVC), polyvinyl alcohol (PVA), polydimethylsiloxane (PDMS), etc.) are frequently used in the fabrication of flexible and wearable electronics. However, the biocompatibility of these polymers over extended periods was not well established and thus they carry a risk of epidermal infection.<sup>[51–53]</sup> In this regard, CS was preferred as it is easy to cast into ultrathin films using solution-processed techniques, possesses excellent mechanical strength, and could be crosslinked to achieve structurally stable films under aqueous exposure. Further, it is biocompatible, self-renewable, biodegradable, anti-microbial, and antimycotic.<sup>[19,54–57]</sup> For mechanical stability and low degradation in an aqueous environment, CS was crosslinked with GO to prepare GO–CS composite which was used as the substrate. Abundant hydroxyl and carboxyl groups in GO reacted with the amine groups ( $-\text{NH}_2$ ) of CS to form stable amide ( $-\text{CONH}_2$ ) linkage.<sup>[54]</sup> Here, high MW CS was used, since its long polymeric chains could provide high mechanical strength to the substrate. To find a suitable stoichiometric composition between GO and CS to obtain a mechanically stable GO–CS composite and to investigate the role of GO in GO–CS, different samples of pure CS, 0.2, 0.5, 0.8, and 1 wt% GO-loaded CS solutions were prepared. To prepare the pure CS substrate, 2 wt% CS solution was prepared by adding 1 g of high molecular wt CS in 50 mL of DI water followed by stirring at 500 rpm @70 °C for 30 min using a magnetic stirrer. Unacetylated CS was insoluble in DI water and formed a uniform particulate solution during stirring. When the powdered CS was uniformly dispersed, the resultant solution was acetylated by adding 9.2 mL of 2% acetic

acid and mixing at 1300 rpm for 24 h at 70 °C until the solution was homogeneously translucent and jelly-like. The acetylated pure CS solution was stored for solution casting.

To prepare 0.2, 0.5, 0.8, and 1 wt% GO-loaded CS solutions, we used 4, 10, 16, and 20 mL of as received GO aqueous dispersion in 46, 40, 34, and 30 mL of DI water, respectively, so that the resultant volumes of GO solutions were 50 mL each. After the GO flakes were well dispersed in the DI water, 1 g of CS was added to each of the GO solutions, along with the same amount of acetic acid, following the aforesaid recipe as described earlier to obtain respective homogeneous brown jelly like solutions. These acetylated GO–CS solutions were aspirated and stored for solution casting.

#### 3.2. Solution Casting of GO–CS and GFN

Different sets of samples with: i) featureless (*p*-) GFN on 0.5 wt% GO-loaded CS, ii) GFN on pure CS, c-GFN on: iii) 0.2 wt%, iv) 0.5 wt%, v) 0.8 wt%, and vi) 1 wt% GO-loaded CS substrates were prepared for various investigations and were labeled as samples S1, S2, S3, S4, S5, and S6, respectively. Each set of the sample consists of six devices for various characterizations. For device fabrication, all the Si carrier substrates were cleaned using oxygen plasma before casting respective CS and GO–CS solutions, as shown in **Figure 2a**. The as-prepared pure CS solution was cast on Si substrate for the fabrication of device S2. To prepare devices with S1, S3–S6, the aspirated 0.2, 0.5, 0.8, and 1 wt% GO-loaded CS solutions were cast on separate Si-carrier substrates for subsequent experiments, as shown in **Figure 2b**. The casted GO–CS solution on Si substrate was subjected to slow air drying at room temperature to: i) avoid the generation of micro-bubbles due to trapped air in the solution, and ii) eliminate any mechanical stress at the edges of the substrate, which could potentially lead to crack formation. The bubble-free GO–CS substrate on the Si carrier wafer was selected for subsequent GFN deposition. The air-drying technique ensured the formation of nanocorrugations on the surface of GO–CS and facilitated the formation of c-GFN with nanosized wrinkles. For S1, the control substrate with featureless surface morphology of GO–CS was prepared by solution casting 0.5 wt% GO-loaded CS solution on Si surface.

Solution-processed GFN dissolved in terpineol solution was used for the deposition of the channel layer. The as-received graphene ink in terpineol was further diluted using the same solvent in a 1:50 ratio by volume and the graphene flakes of average size 5  $\mu\text{m}$  were dispersed using the vortex mixer. A drop of the resultant solution of graphene flakes in terpineol was cast on all substrates and was allowed to dry overnight at 40 °C. The control sample set S1 was prepared by depositing GFN on the smooth side of GO–CS, i.e., the side in contact with the Si surface. The GFN deposited on the featureless GO–CS surface yielded *p*-) GFN on GO–CS substrate. A few layers thick GFN nicely conformed on different variants of nanocorrugated ridges on the GO–CS surface to produce a c-GFN channel in devices S2–S6, as shown in **Figure 2c**. The conductive network of a few layers of GFN was preferred here over the monolayer graphene as the former eliminates complex fabrication processes involving the use of aqueous solutions without sacrificing the conformability to curved substrates.

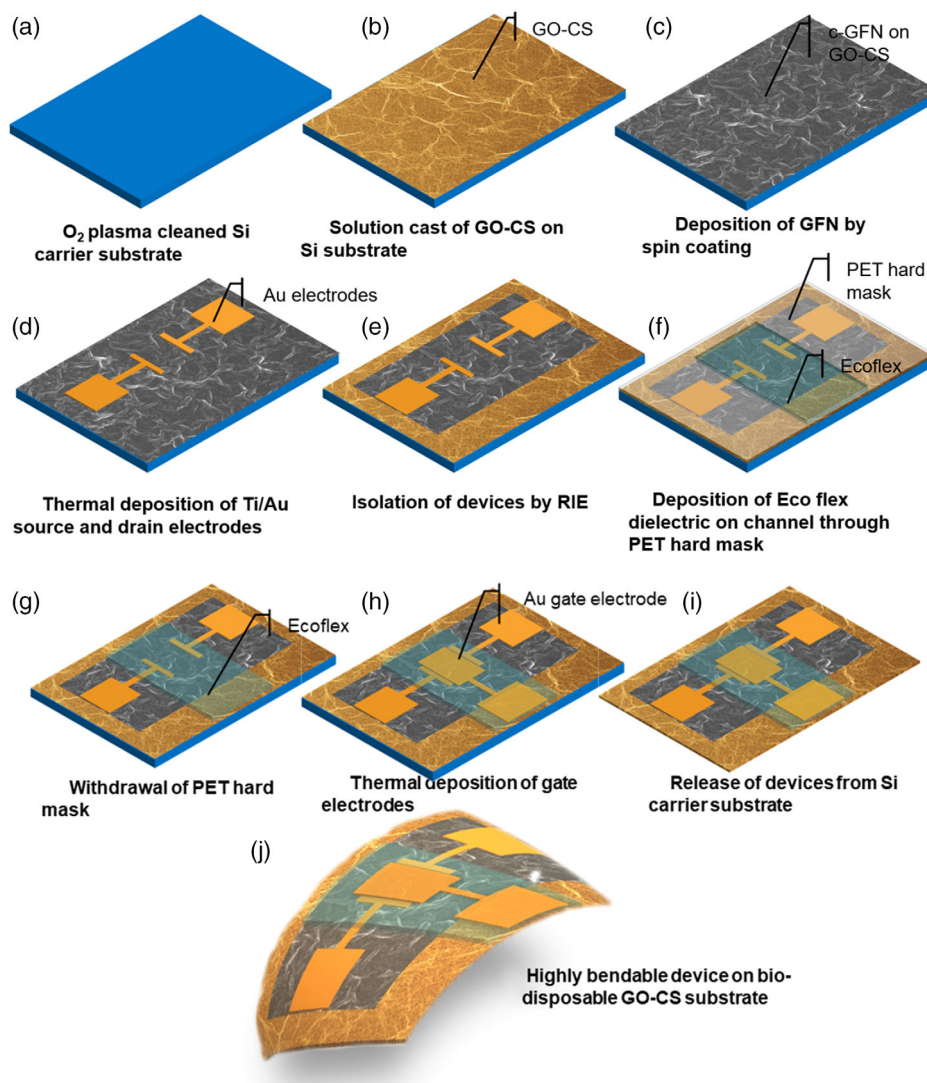


**Figure 2.** Device fabrication: a) Oxygen plasma cleaning of Si carrier for better adherence, b) GO–CS solution casting on Si carrier substrate, c) deposition of graphene flakes solution on GO–CS, d) thermal deposition of Ti/Au source-drain electrodes, e) isolation of devices by RI etching of graphene network layer, f) deposition of Ecoflex dielectric layer using polyethylene terephthalate (PET) hard mask, g) removal of the hard mask, h) thermal deposition of the gate electrode, i) peeling off devices from Si carrier substrate, j) as-fabricated device on bio-disposable GO–CS substrate.

### 3.3. Deposition of Elastomer as Dielectric

The Ti/Au source-drain electrodes (thickness 10/30 nm) on all the sample devices were realized using Ni hard mask, as shown in Figure 2d. The individual devices in a batch were isolated by etching the GFN using a suitable etch mask and reactive plasma for 20 sec, as shown in Figure 2e. The Ecoflex was then deposited on the channel through custom-designed polyethylene terephthalate (PET) hard mask at 5000, 6000, 7000, and 8000 rpm for 60 s, leading to dielectric layers with thicknesses 1  $\mu\text{m}$ , 900, 800, and 700 nm, respectively, as shown in Figure 2f. Different thicknesses of the dielectric layer were explored to find the best combination in terms of the high performance of the sensor and the transistor characteristics. The device with 700 nm dielectric

thickness offered the highest ON/OFF ratio of 15 and hence it was used for the fabrication of the proposed PRESSFET. The sub-micron size dielectric layer was advantageous due to low hysteresis during repetitive operations. The PET hard mask was peeled off from the surface after keeping it at room temperature for 5 min, followed by final curing of Ecoflex at 40 °C for 3 h. Figure 2g schematically shows the Ecoflex dielectric after curing. The Au gate electrodes of thickness 30 nm were deposited on the dielectric layer and aligned over the gap between the source and drain electrodes, as shown in Figure 2h. The device was peeled off from the Si carrier substrate (Figure 2i) after electrical characterization. The released device fabricated on ultrathin GO–CS substrate showed some curling during storage, which may be attributed to the adsorption of ambient moisture.

## 4. Experimental Section

### 4.1. Scanning Electron Microscopy Investigations

Scanning Electron Microscopy (SEM) investigations were performed to evaluate the corrugated morphology of GFN wrinkles and hence the transformation of electronic properties associated with it. SEM studies were also carried out on the inter-electrode space prior to the deposition of the gate dielectric. When the aqueous solution of GO-CS was cast on the carrier Si substrate and allowed to air dry at room temperature, a characteristic surface morphology consisting of a network of nanostructured ridges of width  $\approx 100$  nm was observed. The formation of the characteristic nanocorrugations on the GO-CS surface was attributed to the electrostatic steric repulsion between the edges of adjacent CS-grafted GO flakes during drying, as described in the following.

The long polymeric chains of CS contain copious amount of primary amine  $-NH_2$  groups, which are protonated in a weak acidic medium to form  $-NH_3^+$  chemical moiety, thereby converting CS into a cationic polyelectrolyte,<sup>[58]</sup> while the GO micro-flakes processes dangling functional carboxylic ( $-COOH$ ) groups around their edges as shown in **Figure 3a**. When the GO solution was added to the weakly acidic solution of CS, the polymeric chains of CS containing protonated amino group were grafted at the peripheral edges of the GO flakes through amide linkage,<sup>[59]</sup> resulting in the formation of edge-modified CS-grafted GO flakes in the solution as shown in **Figure 3b**. Due to the abundance of the  $-NH_3^+$  group on the CS chain, the unused protonated amine groups imparted a resultant charge at the edges of GO flakes. The covalent grafting of protonated CS at the periphery of GO flakes increased the electrostatic steric repulsion between neighboring GO flakes, and led to the formation of nanostructured ridges at their interface on drying. The formation of these ridges, as depicted in **Figure 3c**, yielded a nanocorrugated surface morphology on GO-CS. It was observed that the density of nanocorrugations increased with the concentration of GO in GO-CS solution as evident from the SEM images of S3, S4, and S5, as depicted in **Figure 3d–f**, respectively. However, it was further observed from **Figure 3f** that the higher concentration ( $>0.5$  wt%) of GO in CS was found to bring inhomogeneity with evidence of GO agglomerates.

SEM investigations were carried out on all samples after GFN deposition on nanocorrugated GO-CS surface. The surface morphology of the reverse side of the GO-CS substrate in S1 was found to be featureless. Thus, the GFN solution cast on this featureless GO-CS surface yielded featureless *p*-GFN as shown in **Figure 3g**. In sample set S2, the CS substrate possessed no significant corrugations on the surface and the GFN did not exhibit significant crumpled morphology. For corrugated GO-CS surfaces in sample sets S3–S6, the GFN conformed to the nanostructured-ridged morphology of the GO-CS surface to produce *c*-GFN. SEM images in **Figure 3i,j,k,l** show the surface morphology of *c*-GFN in S3, S4, S5, and S6, respectively. Whilst these samples showed the prominent formation of *c*-GFN, their surface morphology differed. To investigate the effect of crumpled nanostructured GFN on the electronic properties of the device we quantitatively studied the role of GO in the formation of a crumpled nanostructure. The crumpledness in GFN was investigated

for sample sets S2–S6 in terms of density (Dcov) of *c*-GFN morphology on the surface of GO-CS and the width (*W*) of the crumpled nanostructured GFN. The sample set S1 was excluded from this investigation. The investigation was carried out using ImageJ software with the SEM images shown in **Figure 3h–l** for S2–S6 (See Section S2, Supporting Information). The Dcov was defined as the percentage of area covered by crumpled nanostructure in the featureless background area (red). The Dcov in S2 was measured to be low (3.8%) due to the absence of GO in the CS substrate. However, the Dcov increased to 54.3% in S3 and 57.7% in S4, saturated to 60.3% for S5, and eventually reduced to 54.4% in S6. Thus, it is evident that the GO-CS surface corrugation and hence Dcov depends on the GO concentration in GO-CS. It was observed that Dcov increased with GO concentration up to 0.5 wt%, after which the Dcov saturated and eventually decreased at 1 wt% GO. Beyond GO concentration = 0.5 wt%, the nanowrinkles/ridges formed on the GO-CS substrate were so dense that the GFN failed to conform to the heavily corrugated surface, resulting in suspended GFN supported by the nanostructured ridges. The suspended GFN morphology was evident from the loss of prominence of *c*-GFN over the nanostructured ridges as observed for S6 in **Figure 3l**. Sample S4 was found with evenly distributed and prominent *c*-GFN over ridged morphology required for enhanced electronic behavior as shown in **Figure 3m**. The crumpled (*c*-) morphology of GFN in the channel transformed the electronic structure of GFN from an  $sp^2$  hybridized state to an  $sp^2$ - $sp^3$  state, resulting in a bandgap opening. The crumpled patterned network developed localized strain at the curved edges of the GFN present over  $\approx 100$  nm high nanostructure-ridges, measured from SEM image in **Figure 3n**. The transformation in the electronic behavior of GFN from zero bandgap semiconductor in planar morphology to finite bandgap semiconductor in its crumpled form could be attributed to the network of strained graphene lattice with  $sp^3$ - $sp^2$  hybridized C-atoms. The strain witnessed by the *c*-GFN conformed over the submicron sized-ridges depend on the curvature of the GFN at its crest. Higher the curvature of the *c*-GFN, the lesser would be the strain on the GFN for bandgap opening. The curvature of the *c*-GFN for samples S2–S6 was investigated in terms of the crest width (*W*) of the *c*-GFN morphology. Reduced *W* signifies the sharp *c*-GFN crest while increased *W* is associated with dull morphology. The *W* measured for samples S3, S4, S5, and S6 was found to be 0.73, 0.54, 0.5, and 0.55  $\mu$ m, respectively. Sharp *c*-GFN nanostructures for samples with high GO concentration could be attributed to the strong electrostatic steric repulsion between adjacent CS-grafted GO microflakes due to reduced inter-microflake distance in an overloaded GO-CS sample. **Figure 3o** shows the variation of Dcov and *W* with the GO concentration in GO-CS. The nanostructural variance in *W* is represented by error bars.

### 4.2. Bio-Disintegration

Our proposed PRESSFET was predominantly composed of GO-CS composite which constitutes the substrate along with limited amounts of graphene micro flakes and metallic Au. Biodegradation of graphene and its derivatives were well established and reported in the literature.<sup>[41,43,60]</sup> Bio-disintegration of devices facilitates their biodegradation

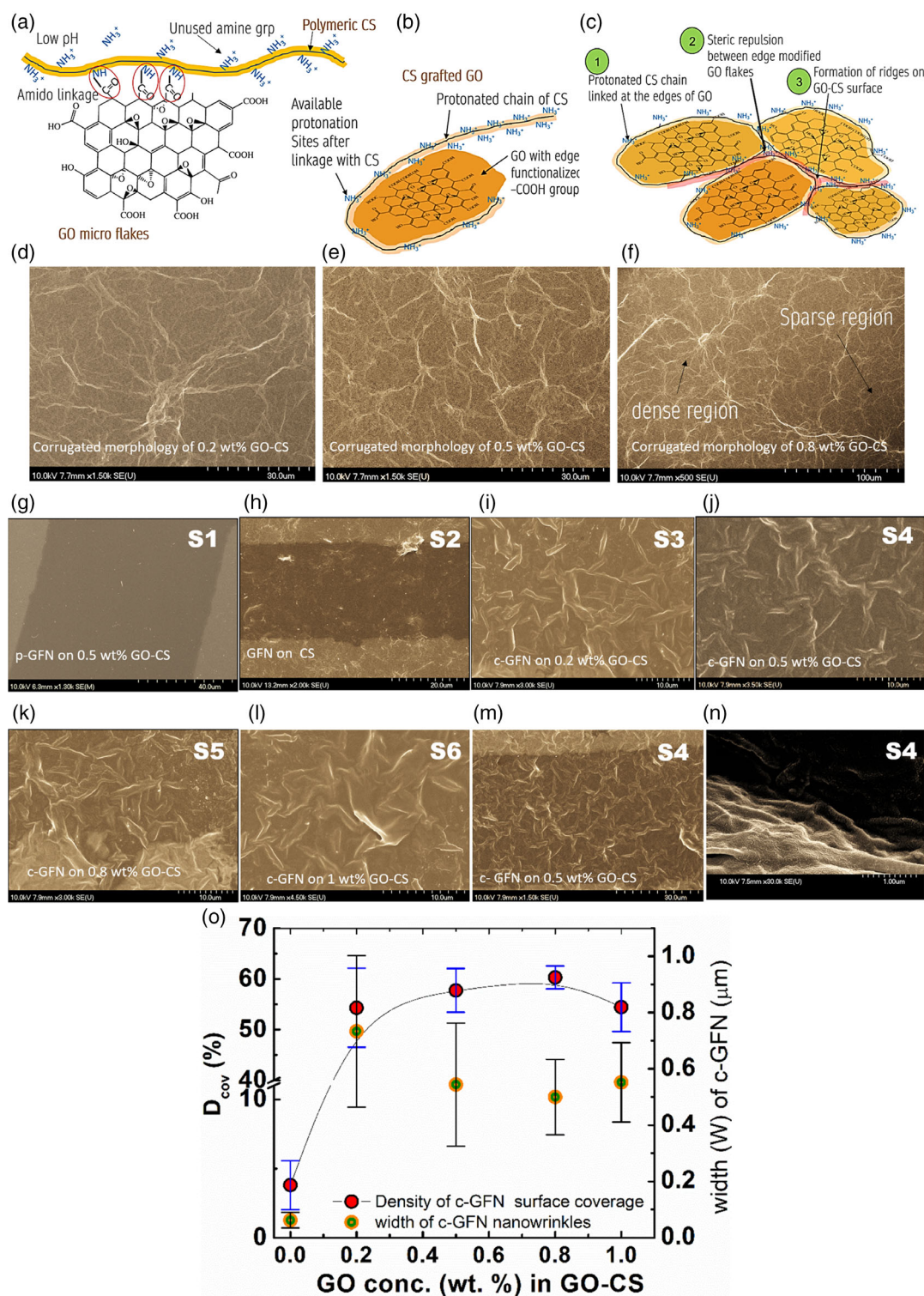


**Figure 3.** Schematic representation of: a) high MW CS and GO microflakes linked together by amide linkage, b) grafting of CS on the edges of GO microflakes, c) formation of nanocorrugated morphology on the GO-CS surface formed due to electrostatic steric repulsion of adjacent CS-grafted GO flakes. SEM images of nanocorrugated GO-CS surface of: d) S3, e) S4, and f) S5. SEM images showing the nanowrinkles of c-GFN in: g) S1, h) S2, i) S3, j) S4, k) S5, l) S6, m) S4 showing the inhomogeneity in nanowrinkle formation, and n) S4 showing its height = 100 nm GFN, and o) plots showing the variations of nanostructural parameters  $D_{cov}$  and  $W$  with the GO concentration in GO-CS.

when disposed of. Since GO–CS forms the major component of the device in terms of weight, the bio-disintegration of GO–CS substrate in an aqueous solution was demonstrated in this work.

The bio-disintegration of the GO–CS substrate was measured in terms of swelling ratio (SR) and is expressed as

$$SR = \frac{W_s}{W_d} \times 100\% \quad (1)$$

where  $W_s$  and  $W_d$  are the weight of swelled and dry samples, respectively. To investigate the effect of GO concentration on the wettability of the GO–CS composite in an aqueous solution the experiments were performed by immersing identically prepared samples S2, S3, S4, S5, and S6 in DI water and weighing the samples several times for each set in the range of time  $t = 0$ –960 min. The experiments with S2 and S3 were terminated after 7, and 180 min respectively on their physical disintegration in an aqueous solution, while for S4, S5, and S6, the experiments were terminated after 980 min when the SR reached their respective saturation wettability. The samples S2, S3, S4, S5, and S6 recorded the highest SR of 25%, 74%, 22%, 15%, and 12%, respectively, as shown in **Figure 4**. It is evident that S4, S5, and S6 suffered a low SR even after 960 mins of exposure to the aqueous medium and thus offered increased mechanical stability than other samples under test. **Figure 4a–c**, inset, shows the images of samples S2, S3, and S4 in a dry state at the start of the experiment while **Figure 4d,e**, inset, show the images of S4 just after dropping in DI water and in fully swelled condition at the end of 980 min, respectively. **Figure 4f** shows the image of S5 at the start of the experiment. This sample was brittle and was resistant to physical disintegration in an aqueous solution after 980 min. It was found that increased incorporation of GO in GO–CS composite provided enhanced mechanical stability to the device in an aqueous solution and would be helpful in

protecting the device against body sweat when in contact with the skin. The increased mechanical stability of the GO–CS in an aqueous solution was chemically confirmed through Fourier Transform Infrared Spectroscopy (FTIR) investigations, where it was observed that the  $-\text{NH}_2$  group of chitosan reacted with the  $-\text{C}=\text{O}$  group of GO to form an amide ( $-\text{NHC}=\text{O}$ ) linkage between the two molecules (See Section S3, Supporting Information). The formation of amide linkage was confirmed by: a) the shift in the  $-\text{NH}$  bending peak of chitosan towards the lower wavenumber to  $1549\text{ cm}^{-1}$  in GO–CS, b) disappearance of the  $-\text{C}=\text{O}$  peak in GO–CS sample, and c) higher intensity of  $-\text{CO}$  stretching vibration peak at  $1060\text{ cm}^{-1}$  as compared to GO at  $1030\text{ cm}^{-1}$ . The increase in GO content in GO–CS reduced the flexibility of the substrate, yet rendering it mechanically stable in an aqueous solution. The sample S4 was preferred over others as it was sufficiently flexible for wearable application and at the same time completely dissolvable in aqueous media in 3 days, as depicted through chronological study in **Figure 4g,h**.

### 4.3. Electrical Characterization of FET

As a semi-metal with a zero-bandgap, the use of graphene is restricted in a few applications where a suitable bandgap is required. The bandgap opening in graphene has also been achieved using bilayer graphene, strained graphene, doping and the chemical functionalization, etc.<sup>[61–67]</sup> The direct bandgap of 930 meV has been reported for graphene with rippled or corrugated morphology and it could be tuned by varying the height and radius of curvature at the crest of the corrugations.<sup>[68]</sup> Since the device channel utilizes multilayered graphene flakes network GFN which has a zero bandgap, the use of corrugated morphology with GFN facilitates bandgap opening and hence

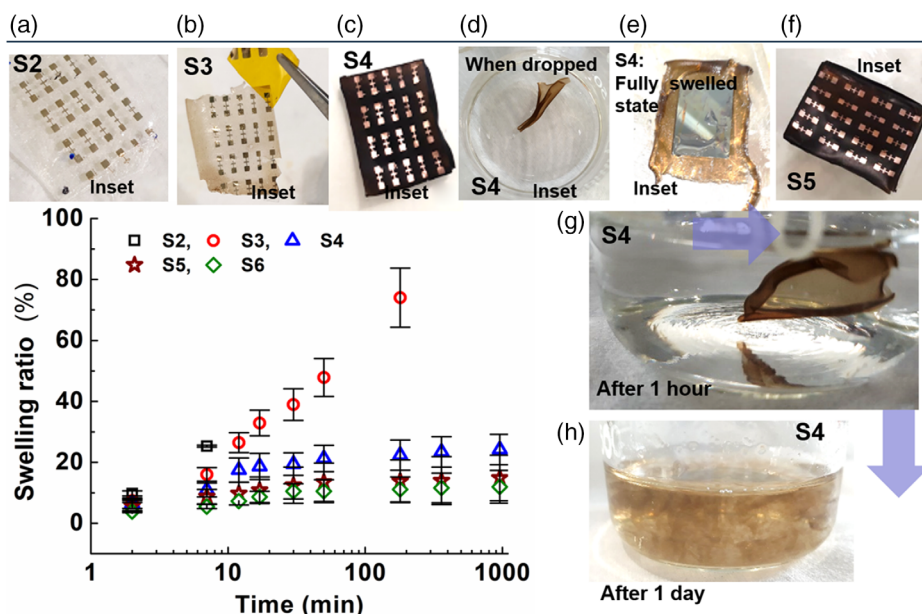


**Figure 4.** The swelling ratio (SR) with time for different compositions of GO–CS, Inset(s): Images of: a) S2, b) S3, c) S4, and f) S5 before putting in an aqueous environment. The physical state of S4 when: d) immersed in aqueous solution and e) at a fully swelled state for SR = 22% after 960 mins of treatment. The GO–CS after: g) 1 h and h) 1 day of immersion showing complete solubility.

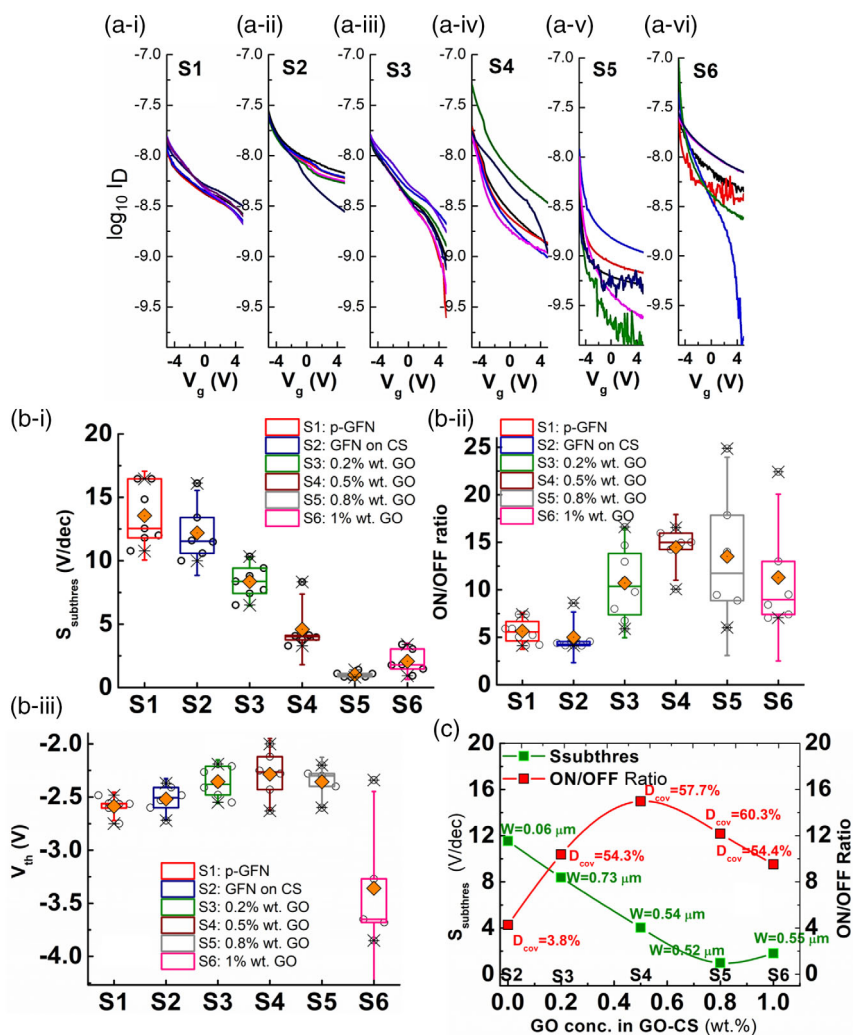


**Figure 5.** a) Log<sub>10</sub> I<sub>d</sub>–V<sub>g</sub> plots of devices with: i) S1, ii) S2, iii) S3, and iv) S4, v) S5, and vi) S6. b) Box plot representation showing the variance in field effect transistor (FET) parameters in terms of: i) S<sub>subthres</sub>, ii) ON/OFF ratio, and iii) V<sub>th</sub> for device sets S1–S6, and c) The variation of mean S<sub>subthres</sub>, ON/OFF ratio with GO concentration in GO–CS.

enhances the switching characteristics of the FET device. The use of crumpled morphology was adopted over other band opening methods due to its simplicity and the ease of preparation with GO–CS substrate. The bandgap in the present case was evaluated through differential conductance versus energy E plots and found to be 800 meV<sup>[69]</sup> (See Section S4, Supporting Information).

#### 4.3.1. Role of Gate Dielectric Thickness *d*

The thickness *d* of the gate dielectric plays an important role in the performance of an FET device. Although low dielectric thickness *d* is preferred for enhanced drain current I<sub>D</sub> modulation by gate voltage V<sub>g</sub>, reduced *d* may affect the sensitivity and operating range of the PRESSFET device. To find a trade-off between the *d* and the FET characteristics, the devices were fabricated with different dielectric thicknesses (*d* = 700, 800, 900, and 1000 nm) on S4: 0.5 wt% GO–CS substrate to investigate the effect of *d* on the FET parameters. The threshold voltages V<sub>th</sub> of devices with

*d* = 700, 800, 900, and 1000 nm were determined from their corresponding G/G' versus gate voltage V<sub>g</sub> curves and found to be –2.13, –2.34, –2.52, and –3 V, respectively (See Section S5, Supporting Information). The subthreshold swing S<sub>subthres</sub> = [Δ log I<sub>d</sub>/Δ V<sub>g</sub>]<sup>–1</sup> was obtained from the inverse of the slope of log I<sub>d</sub> versus V<sub>g</sub> curve. The device with *d* = 700 nm offered low S<sub>subthres</sub> and hence provided sharper switching behavior in comparison to the devices with *d* > 700 nm. Hence, further investigations about the origin and effect of corrugated morphology of GO–CS were carried out for FET devices with *d* = 700 nm.

#### 4.3.2. Effect of Nanostructured Morphology of *c*-GFN on Electronic Structure and Behavior

It was discussed in Section 4.1 that the formation of nanostructured ridges in *c*-GFN played an important role in the bandgap opening in GFN. In this section, we study the effect of the

crumpled morphology mediated bandgap opening on the FET parameters by investigating different samples S1–S6. Six identical devices in each sample set were analyzed statistically. The transfer characteristics plots of different devices were recorded for devices with  $d = 700$  nm in the range of  $V_g = -5$  to  $+5$  V at  $V_d = 50$  mV. The  $\log I_d - V_g$  plots were obtained from their respective transfer characteristics. **Figure 5a–i–vi** shows the  $\log I_d - V_g$  graphs for different sample sets of devices in S1, S2, S3 S4 S5, and S6, respectively. The electron transport and charge carrier mobility in c-GFN was reported to be highly suppressed<sup>[70]</sup> along with nonexistent or fluctuating Dirac point due to subdued weak localization.<sup>[71]</sup> Reduced mobility in the folded and wrinkled c-GFN was attributed to the transport of charge carriers along and across the wrinkles through diffusive transport of charge distributed across the multi-layers of GFN, which increased the ON/OFF ratio of the devices.<sup>[72]</sup> In our work, as the width  $W$  of the wrinkle are in sub-micron range, the performances of devices S2–S6 were statistically investigated in terms of  $S_{\text{subthres}}$ , and ON/OFF ratio and compared with that of sample S1 as shown in **Figure 5b–i,ii** respectively. The  $S_{\text{subthres}}$  were calculated graphically from the inverse of the slope of  $\log I_d$  versus  $V_g$  curve. Low  $S_{\text{subthres}}$  is desirable in FET device for rapid switching characteristics. In contrast, the ON/OFF ratio was calculated as the ratio of the highest  $I_d$  at ON state to the lowest  $I_d$  at OFF state. The ON/OFF ratio relates to the electronic energy gap between two distinct electronic states. High ON/OFF ratio imply effective transition between the two distinct electronic states (ON and OFF states) thereby facilitating efficient switching operations in digital devices. The  $V_{\text{th}}$  for different samples were also investigated as shown in **Figure 5biii**. The acquired data for devices in all the sample sets S1–S6 were denoted by symbol  $\circ$  while the mean of a given data set is denoted by orange solid symbol  $\diamond$ .

To establish that the enhancement in device performance was due to the nanostructured morphology of the c-GFN and is independent of the stoichiometric composition of GO in the GO–CS composite the performance of devices S4 was compared with S1. The device set S4 showed 3.3 times lower  $S_{\text{subthres}}$ , and 2.6 times higher ON/OFF ratio than the devices in set S1. This enhancement in the performance of S4 (with an identical substrate-stoichiometric composition of GO in GO–CS as in S1) was due to the bandgap opening in the former device as compared to S1 (with  $p$ -GFN). The improvement in  $S_{\text{subthres}}$  and ON/OFF ratio was consistent when the degree and the extent of crumpledness, characterized by  $D_{\text{cov}}$  and  $W$ , were systematically varied for different samples S3–S6 by increasing the GO concentration in GO–CS, as shown in **Figure 5b–i–ii**. The variation of device parameters with GO concentration is discussed in Section 4.3.3. Significant improvement in  $V_{\text{th}}$  was also observed in S4 ( $V_{\text{th}} = -2.28$  V) relative to S1 ( $V_{\text{th}} = -2.56$  V) as shown in **Figure 5biii**.

The homogeneity in the distribution and morphology of nanostructured corrugations on the surface of the GO–CS substrate determined the variance in the width  $W$  of the wrinkles. Since the strain at the crest of the wrinkles of c-GFN, and hence the electronic structure depends on  $W$ , any variance in  $W$  may lead to deviation in device performance. The reproducibility in performances for device sets S1–S6 were investigated using box plot representation by determining the interquartile range (IQR) of a

given parameter  $-S_{\text{subthres}}$  and ON/OFF ratio for a fixed set of devices as shown in **Figure 5bi,ii**, respectively. The mean of the acquired data of a particular sample set is represented by solid  $\diamond$ . The variance in acquired data was expressed in terms of IQR, which is calculated as the difference between the upper and lower quartile of the box. Reduced IQR signifies high reproducibility in device fabrication and consistency in electrical outcomes, whereas high IQR depicts inconsistency and unreliability in device performance. The devices S4 and S5 with  $S_{\text{subthres}}$  IQR of 0.41 and 0.3 V  $\text{dec}^{-1}$ , respectively, offered high repetitive consistency around its median  $S_{\text{subthres}} = 3.96$  V  $\text{dec}^{-1}$ . The device S4 offered the highest ON/OFF ratio of 15 with an IQR of 1.3 indicating stable device performance. High IQR in S6 was attributed to the suspended GFN where the variances in  $D_{\text{cov}}$  and  $W$  were high.

#### 4.3.3. Effect of GO Concentration on Device Parameters

The role of GO concentration on the transistor characteristics was investigated on different samples S2–S6 prepared with GO concentration in the range 0–1 wt%. The mean  $S_{\text{subthres}}$  and ON/OFF ratio for all sample data sets S1–S6 were calculated and plotted with the GO concentration as shown in **Figure 5c**. The  $S_{\text{subthres}}$  showed a linear and monotonous decrease in its value with GO concentration in the range 0–0.8 wt% beyond which the value slightly increased. This linear decrease in  $S_{\text{subthres}}$  with GO concentration signified sharp transistor switching behavior for devices with high GO concentration in GO–CS substrates. This is attributed to the nanostructured morphology of the c-GFN including the sub-micron sized  $W$  of the crumpled GFN ridges and their 100 nm height. This nanostructured morphology on the c-GFN produced quantum confinement in the c-GFN channel, leading to the bandgap opening<sup>[71]</sup> and quantization of energy levels.<sup>[73]</sup> These nanocrumpled wrinkles on the c-GFN formed a network of 1D quantum confinement structures which efficiently confine charge carriers, without inducing significant inter-valley scattering.<sup>[74]</sup> Twisted graphene layers in a thick film network also contributes to quantum confinement in c-GFN.<sup>[75]</sup> Higher the confinement of charge carriers in the c-GFN, lower would be the  $S_{\text{subthres}}$  of the device. Due to reduced width  $W$  of the nanostructured ridges on c-GFN, sample S5 showed the lowest  $S_{\text{subthres}} = 0.97$  V  $\text{dec}^{-1}$  as compared to other devices.

The mean ON/OFF ratio improved from 5 in set S2, through 10.7 in S3 to 14.5 in S4, and subsequently dropped to 12.17 and 9.72 for S5 and S6, respectively. The ON/OFF ratio increased monotonically with GO concentration in the range 0–0.5 wt% GO loading in GO–CS beyond which the value was sharply reduced. This increase in the ON/OFF ratio may be attributed to the increased c-GFN coverage  $D_{\text{cov}}$  on the channel. These crumpled nanostructured GFN facilitate the bandgap opening in the devices<sup>[16]</sup> and hence led to enhanced ON/OFF ratio. The lattice strain in c-GFN due to large curvature at the crest of the wrinkle generated hyperbolic energy dispersion which eventually resulted in bandgap opening. Moreover, strained c-GFN at the wrinkle curvature produced zero-field Landau level like quantization and valley polarization with a large bandgap.<sup>[71]</sup> Thus, high curvature assisted strained c-GFN and hence high

Dcov imparted superior ON/OFF ratio to sample S4 than its counterparts. The obtained ON/OFF ratio in our proposed device S4 was higher than that reported in works.<sup>[12,13,15]</sup> However, the GFNs show increased resistivity and reduced mobility due to the diffusive transport of charge carriers along and across the curved (strained) regions.<sup>[76]</sup> The ON/OFF ratio was reduced for GO concentration >0.5 wt%, as observed for samples S5 and S6. This may be attributed to the suspended GFN morphology with reduced strain in GFN lattice at the wrinkle curvature. The device set S4 offered a lowest  $V_{th} = -2.28$  V than the other devices, respectively, and thus facilitated switching at lower  $V_g$  as depicted in Figure 5biii. The device S2 exhibited poor  $S_{subthres}$  and ON/OFF ratio due to the absence of crumpled morphology in GFN channel, leading to subdued FET device characteristics. Thus, the incorporation of GO in GO–CS substrate played a pivotal role in the formation of corrugations in GO–CS substrate morphology, which facilitate the formation of the crumpled graphene channel for enhanced device characteristics. Due to enhanced ON/OFF ratio (=15), low  $V_{th} = -2.3$  V, and good  $S_{subthres} = 4$  V dec<sup>-1</sup>, device S4 was most suitable for our application as a pressure responsive switching device. The device characteristics can be tuned by regulating the GO concentration in GO–CS as depicted in Figure 5c.

#### 4.3.4. Environmental Degradation

The devices often suffer from environmental degradation and therefore it is important to estimate their long-term performance and shelf life. The environmental degradation ( $D$ ) studies were performed with devices in set S4 by preserving the sample in air at room temperature over a period of 7 weeks, in which the transfer characteristics of the devices were recorded at  $V_d = 50$  mV in the  $V_g$  range of  $-5$  to  $5$  V at an interval of 1 week. Respective  $\log I_d$ – $V_g$  plot was obtained from each transfer characteristics curve at a given week as shown in Figure 6a. The ON/OFF ratio and the  $S_{subthreshold}$  for different weeks were calculated and plotted with time as shown in Figure 6b. Since the ON and OFF state  $I_D$  play an important role in the sensor performance the degradation  $D_n$  at the end of the  $n$ th week was expressed in terms of variation in the ON/OFF ratio of the device over the given time interval as

$$D_n = \frac{(\text{ON/OFF}|_0 - \text{ON/OFF}|_n)}{\text{ON/OFF}|_0} \times 100\% \quad (2)$$

where  $\text{ON/OFF}|_0$  denotes the ON/OFF ratio during commencement at  $t = 0$  week and  $\text{ON/OFF}|_n$  denotes the ON/OFF ratio at the end of  $n$ th week

The device suffered monotonic degradation over time reaching a 20% degradation at around 3 weeks of operation, as shown in Figure 6b. Considering the shelf-life of the device with a tolerable degradation of 20%, the experiments showed that the devices can be stored in normal atmospheric conditions for a maximum period of 3 weeks for best device performance. This duration is good for a device that is designed to naturally degrade, but could be improved with suitable encapsulation, if required.<sup>[19]</sup> Following our observations that the: 1) incorporation of GO extends the biodegradability of the device (Section 4.2), 2) the presence of crumpled GFN as a channel enhances the device characteristics (Section 4.3.2), and the 3) density of crumpled structures improves the FET performance (Section 4.3.3), we investigate the performance of the devices in response to pressure.

#### 4.4. PRESSFET Performance

In this section, we measure the pressure sensing performance of devices in sets S1, S3, and S4 under static and dynamic loadings in the range of 500–2500 Pa using the probe station connected to the semiconductor parameter analyzer 4155C (Agilent Technologies, Inc.). The response of external pressure  $P$  was investigated in the range  $P = 500$ – $2500$  Pa (with an incremental step of 500 Pa), for a total sampling time of 40 s on devices S1, S3, S4, and S5. Experiments with S2 were not performed as it is not suitable for wearable applications due to high SR. The investigations were not carried out on S6 as well because; a) the FET characteristics were observed to be poor and b) the suspended GFN layer in response to external  $P$  often generated cracks which yielded inconsistent device performance when operated under multiple cycles. As the developed device is a  $p$ -type enhancement mode GFET, the pressure responses for respective sets were determined by pre-biasing the device at their respective  $V_{th}$  to operate it in the ON state. The pressure responses of various devices were recorded with devices operated at  $V_d = 50$  mV as shown in Figure 7a. Each loading cycle included the holding and relaxation times of 4 s. The response time was determined as the time taken for the output signal to achieve 90% of its full-scale output and was found to be around 1.2 s.

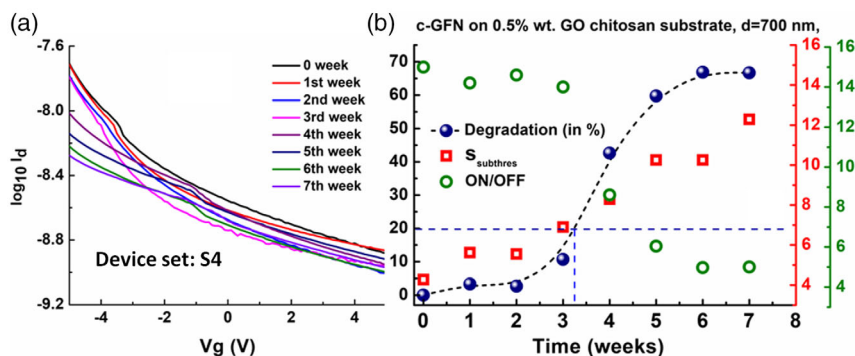


**Figure 6.** a) Semilog plot of  $\log I_d$  versus gate voltage  $V_g$  of S4 for a time interval of 7 weeks. b) Plot of  $S_{subthres}$ , ON/OFF ratio, and the degradation  $D_n$  at the  $n$ th week with time showing the shelf-life to be 3 weeks assuming a tolerance of 20%.

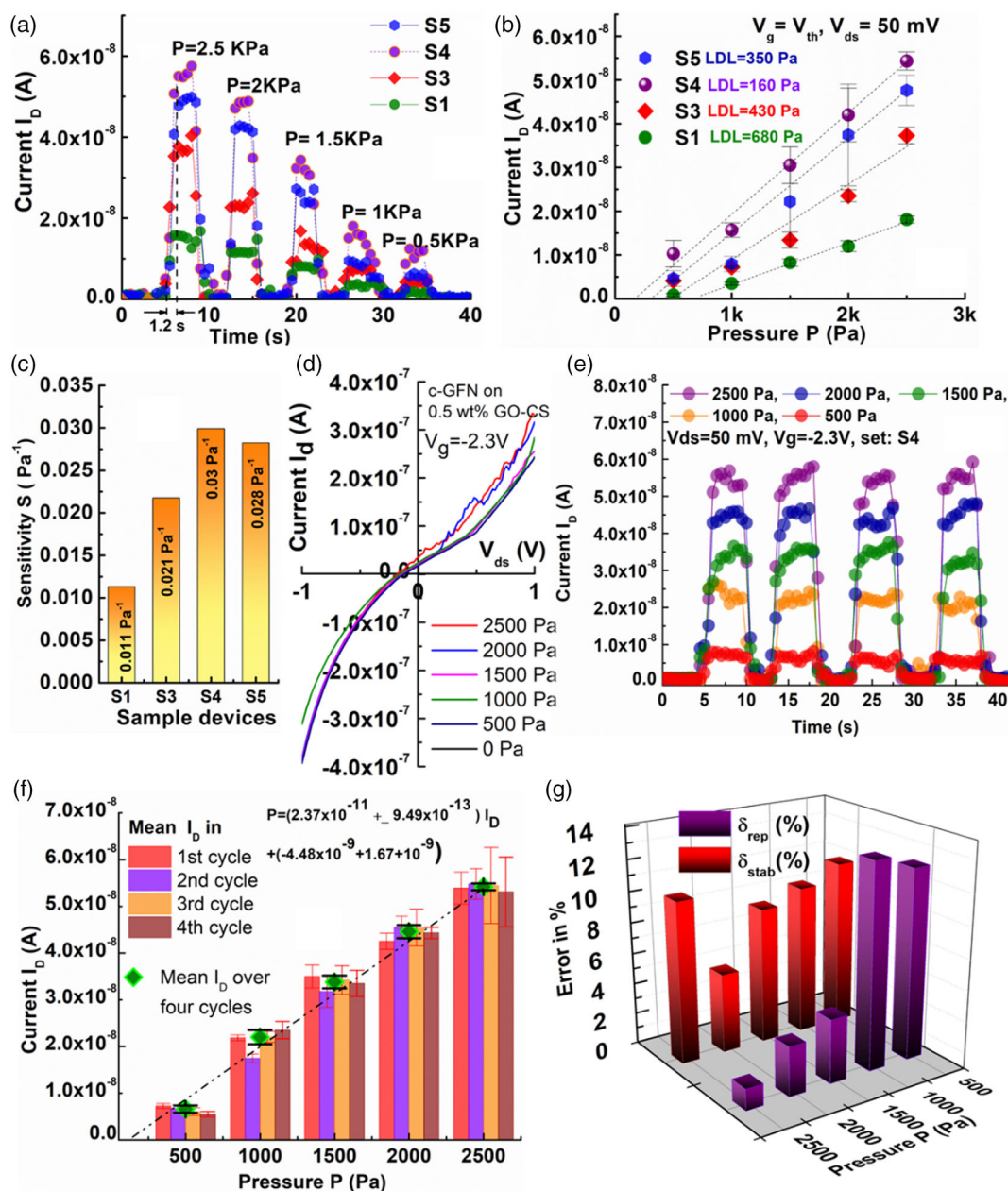


**Figure 7.** a) Output current  $I_D$  versus time plot for different samples under dynamic loadings in the experimental range 500–2500 Pa. b) Comparative study of  $I_D$  versus  $P$  calibration curves for different samples. c) Column bar graph comparing the sensitivities of different devices. d) Output characteristics curves for S4 at different  $P$ -loadings. e) Dynamic response of the device under repetitive loading in the range 500–2500 Pa. f) Data analysis bar graph showing the steady state mean  $I_D$  for different repetitive cycles and loadings for the reconstruction of the  $I_D$  versus  $P$  calibration curve for the given device.

The measurements were repeated with five identical samples for each set of devices and the mean  $I_D$  was plotted in Figure 7b. The variations in the measured data for the given set of samples were depicted as error bars. The sample device S4 offered the highest sensitivity  $S = 0.03 \text{ Pa}^{-1}$  in the experimental range. The comparative study of the sensitivities of different devices is shown in Figure 7c. The value of  $S$  obtained for PRESSFET: S4 was benchmarked with other reported graphene flakes based pressure sensors and our device was found to exhibit higher (by a factor of  $\approx 100$ ) sensitivity.<sup>[77,78]</sup> The LDL was estimated from the

respective calibration curves of the devices by extrapolating the linear calibration curves to the  $I_D = 0$  line as shown in Figure 7b. The LDLs of devices S1, S3, S4, and S5 were found to be 680, 430, 160, and 350 Pa, respectively. The device S4 showed 2.5 times better sensitivity and more than 4.3 times lower LDL as compared to S1. The results clearly showed that well-conformed c-GFN with large  $D_{\text{cov}}$  and sharp nanowrinkles led to significant improvement in the device performance in S4. Figure 7d shows the output characteristics of the device in the  $V_{\text{ds}}$  range of  $-1$  to  $1$  V at  $V_g = -2.3$  V for different loads in

the experimental range of operation. With increasing pressure, the dielectric thickness decreased, the slope of the output characteristics curve increased and the output current  $I_D$  improved. The undulations in the curves appeared due to the transformation in electronic behavior of  $p$ -GFN to its corrugated morphology and the appearance of  $I_D$  strained network as manifested in the emergence of Van Hove singularities described in Section S4, Supporting Information.

Since the proposed device was designed for wearable applications and required stable and consistent operation in a slender dynamic range for hands-free activation, the device was evaluated for preciseness during operation. The preciseness in the measurement was measured in terms of repeatability and stability error the device S4 when it was subjected to repetitive loadings ( $P = 500, 1000, 1500, 2000,$  and  $2500$  Pa) with alternative hold and relax cycles of 5 s each for a total sampling time of 40 s as shown in Figure 7e. The device was biased at  $V_{ds} = 50$  mV and  $V_g = -2.3$  V. The electrical stability in the acquired data was expressed as stability error in  $I_D$  for each hold state of loading cycles. The stability error for a given value of  $P$  at a particular repetitive cycle was calculated using  $\delta_{stab} = \frac{[SD]_n}{[I_d]_{ssm}} \times 100\%$ , where  $[SD]_n$  denotes the standard deviation about the steady-state mean  $I_d (= [I_d]_{ssm})$  of the data acquired during the holding time in the  $n$ th repetitive cycle. The  $\delta_{stab}$  for all four cycles and different loadings are represented by error bars (in red) about their respective  $[I_d]_{ssm}$  (represented by column bars) as shown in Figure 7f. The  $<10\%$  average stability error  $\delta_{stab}$  over different repetitive cycles (Figure 7g) signifies excellent electrical stability of the output signal. The repeatability error obtained using  $\delta_{rep} = \frac{\text{stand. dev. of } [I_d]_{ssm}}{\text{Mean } [I_d]_{ssm}} \times 100\%$  was found to be 12% and

13% for  $P = 500$  and  $1000$  Pa, respectively, but it decreased to 1.3% for high  $P = 2000$  Pa. The  $[I_d]_{ssm}$  was obtained from the steady-state data acquired for different loading cycles at fixed  $P$  values. The values of  $[I_d]_{ssm}$  for different  $P$  loadings and their corresponding errors (error bars in black) are depicted in Figure 7f. The proposed device due to its enhanced switching property and low LDL is used as a control switch for robotic movements. Since the device was fabricated with biocompatible and bio disposable materials, it was most suited for wearable applications.

## 5. Robotic Applications

Ultrathin and skin-friendly PRESSFET are attractive for wearable applications. The hands-free control using PRESSFETs can potentially benefit amputees and partially paralyzed victims who have partially or wholly lost voluntary control over their limbs. The demonstration of hands-free control of robotic devices was performed with device S4. For the demonstration, identical PRESSFETs were attached to the inner sides of a pair of eyeglasses to maintain contact with the temple area of the face, as shown in Figure 8a–i. The devices captured the voluntary flexure and relaxation movements of the temporalis muscle (Figure 8a–ii) through the pressure exerted on them. The device was switched to an ON state when the temporalis muscles on one side of the face were flexed (with the withdrawal of the mandible (lower jaw)). The device remained in its OFF state when the muscles were in a relaxed state. The devices were operated in  $p$ -type enhancement mode where the gate  $G$  electrode was negatively biased at  $V_g = -2.3$  V relative to the source  $S$

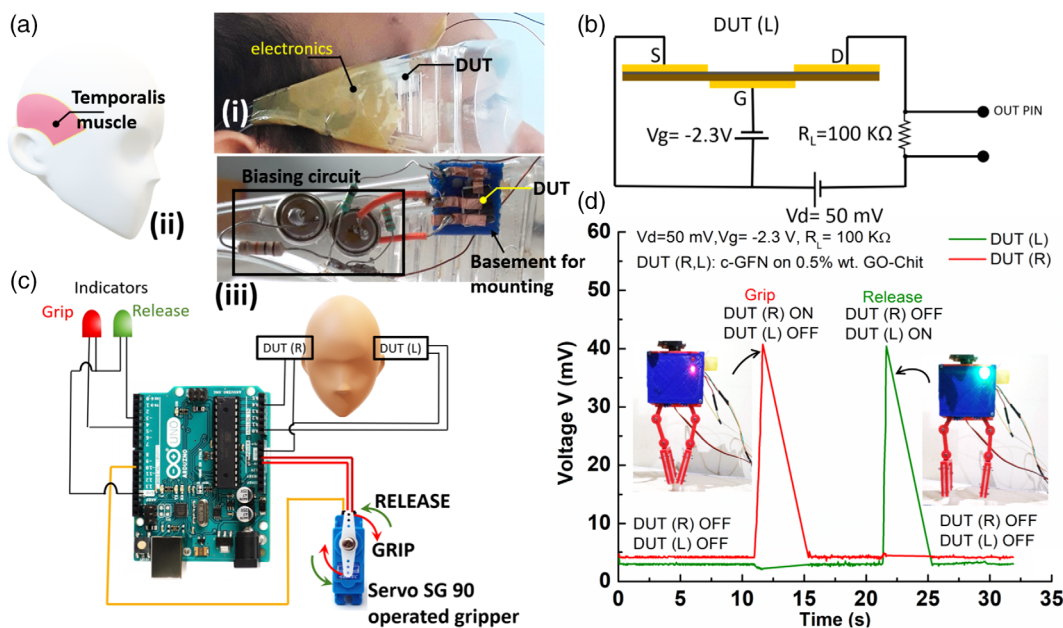


**Figure 8.** Image showing: a-i) Device under test (DUT) and associated electronics on the eyeglasses for hands-free control of equipment, a-ii) illustrative representation of the temporalis muscle of the face, a-iii) DUT connected to the biasing circuit for operation under enhancement mode. b) Circuit diagram of the DUT under biased state, c) schematic diagram showing the integration of a pair of DUT, electronic machine in the form of a microservo, microcontroller (Arduino Uno) and the indicators, and d) output voltage  $V_{RL}$  versus time plot for both DUT (R) and DUT (L) demonstration of the operation of the DUTs.

electrode. The DUT on either side of the temple was suitably biased for operation using the voltage divider circuits by separate button batteries for  $V_g$  and  $V_d$  as shown in Figure 8a–iii. The source  $S$  and the drain  $D$  electrodes were biased at  $V_d = 50$  mV and were connected to load through high load resistance  $R_L = 100$  K $\Omega$ , as shown in Figure 8b. The hands-free control based on these devices was demonstrated by using a laboratory designed: a) robotic gripper with two operational functionalities and b) robotic car with three operational functional modes as described in the following subsections.

### 5.1. Hands-Free Robotic Gripper

The hands-free control of the robotic gripper was demonstrated through two independent operational modes—A) gripping mode and B) release mode. In mode A, the device under test (DUT) was on the right (R) side of the face and triggered the ON state by flexing the right temporalis muscle at which the gripper arms converged toward each other to grasp the object. Under mode B, the DUT on the left (L) side of the face was activated by flexing the left temporalis muscle at which the gripper arms retracted to release the object. The DUT (L) and DUT (R) were in the OFF state in mode A and mode B operation, respectively. The biased DUT (R) and DUT (L) were connected to a microservo (SG 90) to control their clockwise and anti-clockwise movements. The DUTs (L,R) were connected to the Light Emitting Diode (LED) indicators through Arduino Uno as illustrated in Figure 8c. The electrical connections and data acquisition are described in detail in the Section 6, Supporting Information. The servo was programmed to operate in clockwise and anti-clockwise directions with the voltage drop across  $R_L$  ( $V_{RL}$ ). Figure 8d shows

the  $V_{RL}$  versus time graph for both DUT (R) and DUT(L) depicting the gripping and release operations at their respective ON states as depicted by corresponding red and green LED indicators. The consistency in the switching characteristics of DUT (R) and DUT (L) was investigated through 12 successive cycles of alternating gripping (red) and releasing (green) operational tasks as shown in Figure 8e.

### 5.2. Hands-Free Robo-Vehicle

DUT (L,R) was also utilized to demonstrate the hands-free control of a robotic vehicle. Here, the devices supported three operational functions—Mode (A) motion in the forward direction, Mode (B) turning the vehicle in the right direction, Mode (C) turning it in the left direction, and Mode D vehicle at standstill. In Mode (A) and (D), both the DUT (R) and DUT (L) were simultaneously at their ON and OFF state, respectively. In Mode (B) and (C), the DUT(R) and DUT (L) were triggered to their ON state (ensuring that the DUT at the opposite side was OFF) by flexing the right and left temporalis muscles, respectively. The DUT (R) and the DUT (L), through the microcontroller (Arduino Uno board), were connected to two high torque servos MG995 which received electronic signals from the devices when they were triggered to their corresponding ON state, as shown in Figure 9a. The pair of servos, aligned in mirror image arrangement, served as the frontal wheels of the robotic vehicle while a pair of rollers without electronic control constitutes the rear wheels. When both the servos rotated in an anti-clockwise direction the robotic vehicle moved forward (Figure 9b–i). The vehicle turned toward the right when the left servo rotated in the anti-clockwise direction and the right servo in

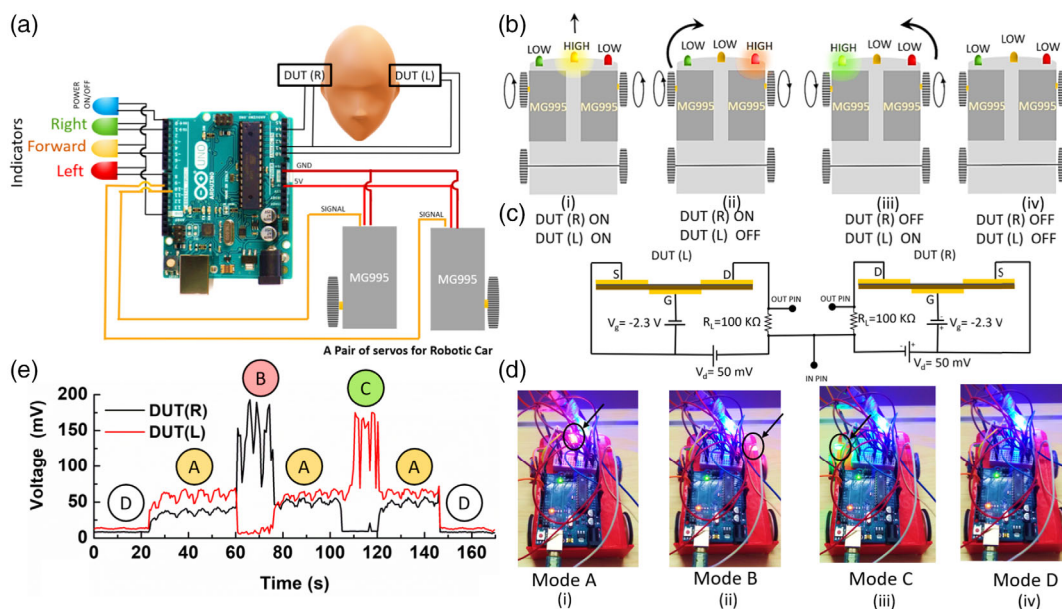


**Figure 9.** a) Circuit diagram of a pair of DUT connected to a pair of continuous 360° rotation servo motors integrated to operate as a robotic vehicle through microcontroller (Arduino Uno) and the indicators. b) Schematic of different modes of functionalities: i) Mode A: moves forward, ii) Mode B: turn right, iii) Mode C: turn left, and iv) Mode D: stop showing the corresponding electronic states of DUT (R) and DUT (L). c) Circuit diagram of DUT (R) and DUT (L) connected to each other under biased state and d) images of the robotic vehicle under functional Modes A–D. e) Output voltage  $V_{RL}$  versus time plot for both DUT (R) and DUT (L) showing the HIGH states of respective functional modes and indicators.

the clockwise direction, as depicted in Figure 9b–ii. Conversely, anticlockwise rotation of the right servo and clockwise rotation of the left servo turned the vehicle towards the left (Figure 9b–iii). The vehicle was stationary when both the DUTs are at OFF state (Figure 9b–iv). Thus, the microprocessor was so programmed to allow DUT (R) ON (with DUT (L) kept at its OFF state) to trigger the left servo to perform anticlockwise rotation while the right servo executed clockwise rotation to turn the robotic vehicle towards the right. Similarly, the microprocessor was pre-programmed to turn the vehicle toward the left when DUT (L) was switched ON, following the converse analogy. The devices were biased in the same way and worked in the *p*-type enhancement mode as discussed in the earlier section. The devices were connected in such a way that they possessed separate input terminals but shared a common output terminal as shown in Figure 9c. Since the devices DUT (R) and DUT (L) were internally connected, the  $V_{RL}$  for both devices showed a reduction in value when both devices were switched to their ON state. In response to various sets of electronic signals received by the microcontroller the robotic vehicle operated at: i) Mode A, as indicated by the glowing yellow indicator, ii) Mode B, as indicated by the glowing red indicator, iii) Mode C as indicated by glowing green indicator, and iv) Mode D, when all the indicators are OFF. The various modes of operation were demonstrated as shown in Figure 9d. Figure 9e shows the  $V_{RL}$  versus time plot for DUT (R) and DUT (L) demonstrating different output signals which trigger various sets of operations as described in Mode A–D operations. The proposed wearable devices can be used with wireless communication for hands-free control as reported in ref. [79].

## 6. Conclusions

The work reported the development of ultrathin PRESSFET on a 3  $\mu\text{m}$  thick bio-disposable GO–CS substrate. The top gated FET was fabricated with Ecoflex as the dielectric material (thickness 700 nm) and c-GFN as the channel. The proposed PRESSFET with a c-GFN channel possessed 2.6 times enhanced ON/OFF ratio and 3.3 times reduced subthreshold swing  $S_{\text{subthres}}$  relative to the devices having featureless planar (*p*-) GFN as the channel. This enhancement in the ON/OFF ratio facilitated the use of solution-processed c-GFN-based PRESSFET as switching devices for wearable electronics. The enhancement in device characteristics was attributed to the formation of crumpled morphology of the GFN which modified the electronic behavior of the GFN. The crumpled morphology was achieved by allowing the solution-processed GFN to conform over the nanocorrugated surface of GO–CS. The nanocorrugations on the GO–CS substrate were developed due to electrostatic steric repulsion between adjacent CS-grafted GO microflakes during drying. The nanostructured morphology of the c-GFN produced quantum confinement in the channel, which led to the bandgap opening and quantization of energy levels. Moreover, the lattice strain in c-GFN due to large curvature at the crest of the wrinkle generates hyperbolic energy dispersion resulting in bandgap opening. The degree of crumple and the electronic structure of c-GFN can be tuned by changing the GO concentration in GO–CS. It was found that 0.5 wt% GO- concentration in GO–CS led to nanostructured morphology

with  $\approx 0.54 \mu\text{m}$  wide and  $0.1 \mu\text{m}$  high nanowrinkles and a bandgap opening of  $\approx 800 \text{ meV}$ . The as fabricated device achieved a  $S_{\text{subthres}} = 3.96 \text{ V dec}^{-1}$  and ON/OFF ratio = 15 thereby providing good switching between distinct LOW and HIGH states under external applied pressure *P*. The device exhibits high sensitivity  $S = 2.64 \text{ KPa}^{-1}$  in the range  $P = 0.5\text{--}2.5 \text{ KPa}$ , excellent electrical stability with max. error of 10% and output repeatability with max. error of 13%. The application of PRESSFET was also demonstrated as a wearable switching device for the operation of hands-free control of robotic gripper and a robotic vehicle. The hands-free control was achieved by attaching a pair of PRESSFET on the left (L) and right (R) side of the temple regions of the face and was denoted as device under test DUT (L) and DUT (R), respectively. The DUTs (L, R) were triggered ON and OFF by flexure and relaxation, respectively, of the temporalis muscles near the ears. The servo motors were operative at the ON state and ceased to work under rest (OFF) state. Based on the complexity of operation, more than a pair of devices can be utilized to potentially benefit paralytic or limb loss patients. The device was fabricated mostly using eco-friendly materials which can degrade in soil over a period of 3 months, thereby making it attractive for future green technology.

## Supporting Information

Supporting Information is available from the Wiley Online Library or from the author.

## Acknowledgements

This work was supported in part by the Engineering and Physical Sciences Research Council (EPSRC) through Engineering Fellowships for Growth (EP/R029644/1) and Heteroprint Programme Grant (EP/R03480X/1) and Academy of Medical Sciences through Newton International Fellowship (NF161567).

## Conflict of Interest

The authors declare no conflict of interest.

## Author Contributions

A.P. and R.D. conceptualized the idea and planned the study. A.P. and N.Y. fabricated the devices. A.P. characterized the devices, analyzed the data analysis, and performed robotic experiments. All authors contributed to the manuscript writing. R.D. acquired the funding, reviewed and edited the manuscript, and provided overall supervision of the project.

## Data Availability Statement

The data that support the findings of this study are available from the corresponding author upon reasonable request.

## Keywords

crumpled graphene, degradable electronics, flexible electronics, graphene, pressure sensors

Received: July 1, 2022  
Revised: August 21, 2022  
Published online: September 29, 2022

- [1] D.-H. Kim, J. Viventi, J. J. Amsden, J. Xiao, L. Vigeland, Y.-S. Kim, J. A. Blanco, B. Panilaitis, E. S. Frechette, D. Contreras, D. L. Kaplan, F. G. Omenetto, Y. Huang, K.-C. Hwang, M. R. Zakin, B. Litt, J. A. Rogers, *Nat. Mater.* **2010**, *9*, 511.
- [2] Y. Jeong, J. Park, J. Lee, K. Kim, I. Park, *ACS Sensors* **2020**, *5*, 481.
- [3] Kenry, J. C. Yeo, C. T. Lim, *Microsyst. Nanoeng.* **2016**, *2*, 16043.
- [4] Y. Yogeswaran, E. S. Hosseini, R. Dahiya, *ACS Appl. Mater. Interfaces* **2020**, *12*, 54035.
- [5] O. Ozioko, P. Karipoth, M. Hersh, R. Dahiya, *IEEE Trans. Neural Syst. Rehabil. Eng.* **2020**, *28*, 1344.
- [6] M. Ion, S. Dinulescu, B. Firtat, M. Savin, O. N. Ionescu, C. Moldovan, *Sensors* **2021**, *21*, 2075.
- [7] R. Dahiya, D. Akinwande, J. S. Chang, *Proc. IEEE* **2019**, *107*, 2011.
- [8] O. Ozioko, R. Dahiya, *Adv. Intell. Syst.* **2022**, 2100091.
- [9] S. Ullah, X. Yang, H. Q. Ta, M. Hasan, A. Bachmatiuk, K. Tokarska, B. Trzebicka, L. Fu, M. H. Rummeli, *Nano Res.* **2021**, *14*, 3756.
- [10] M. Kumar, D. K. Sharma, *Innovat. Res.* **2014**, *9*, c37.
- [11] L. Ma, J. Wang, F. Ding, *ChemPhysChem* **2013**, *14*, 47.
- [12] A. M. Mahjoub, A. Nicol, T. Abe, T. Ouchi, Y. Iso, M. Kida, N. Aoki, K. Miyamoto, T. Omatsu, J. P. Bird, D. K. Ferry, K. Ishibashi, Y. Ochiai, *Nanoscale Res. Lett.* **2013**, *8*, 22.
- [13] N. N. M. Maidin, et al., *Int. J. Nanoelectron. Mater.* **2018**, *11*, 123.
- [14] S. Wang, Z. Hossain, Y. Zhao, T. Han, in *Graphene Field-Effect Transistor Biosensors*, Springer, Singapore **2021**, pp. 87–92.
- [15] S. Papamatthaiou, P. Estrela, D. Moschou, *Sci. Rep.* **2021**, *11*, 9815.
- [16] V. M. Pereira, A. H. Castro Neto, H. Y. Liang, L. Mahadevan, *Phys. Rev. Lett.* **2010**, *105*, 156603.
- [17] J. Luo, H. D. Jang, T. Sun, L. Xiao, Z. He, A. P. Katsoulidis, M. G. Kanatzidis, J. M. Gibson, J. Huang, *ACS Nano* **2011**, *5*, 8943.
- [18] F. Xu, X. Li, Y. Shi, L. Li, W. Wang, L. He, R. Liu, *Micromachines* **2018**, *9*, 580.
- [19] E. S. Hosseini, L. Manjakkal, D. Shakhiviel, R. Dahiya, *ACS Appl. Mater. Interfaces* **2020**, *12*, 9008.
- [20] S. Vishniakou, R. Chen, Y. G. Ro, C. J. Brennan, C. Levy, E. T. Yu, S. A. Dayeh, *Adv. Mater. Technol.* **2018**, 1700279, 1.
- [21] B.-Y. Lee, J. Kim, H. Kim, C. Kim, S.-D. Lee, *Sens. Actuat. A: Phys.* **2016**, *240*, 103.
- [22] I. Khodasevych, S. Parmar, O. Troynikov, *Sensors*, **2017**, 17.
- [23] J. Kim, E. F. Chou, J. Le, S. Wong, M. Chu, M. Khine, *Adv. Health. Mater.* **2019**, *8*, 1900109.
- [24] S. Hannah, A. Davidson, I. Glesk, D. Uttamchandani, R. Dahiya, H. Gleskova, *Org. Electron.* **2018**, *56*, 170.
- [25] A. Vilouras, A. Christou, L. Manjakkal, R. Dahiya, *Materials* **2020**, *2*, 2601.
- [26] T. Sekitani, U. Zschieschang, H. Klauk, T. Someya, *Nat. Mater.* **2010**, *9*, 1015.
- [27] C. Yan, W. Deng, L. Jin, T. Yang, Z. Wang, X. Chu, H. Su, J. Chen, W. Yang, *ACS Appl. Mater. Interfaces* **2018**, *10*, 41070.
- [28] F. A. Viola, A. Spanu, P. C. Ricci, A. Bonfiglio, P. Cosseddu, *Sci. Rep.* **2018**, *8*, 8073.
- [29] E. S. Hosseini, S. Dervin, P. Ganguly, R. Dahiya, *ACS Appl. Bio Mater.* **2020**, *4*, 163.
- [30] S. Dervin, P. Ganguly, R. S. Dahiya, *IEEE Sens. J.* **2021**, *21*, 26226.
- [31] Z. Li, I. A. Kinloch, R. J. Young, K. S. Novoselov, G. Anagnostopoulos, J. Parthenios, C. Galiotis, K. Papagelis, C.-Y. Lu, L. Britnell, *ACS Nano* **2015**, *9*, 3917.
- [32] S. Deng, V. W. Berry, *Mater. Today* **2016**, *19*, 197.
- [33] J. Vaisekauskaite, P. Mazurek, S. Vudayagiri, A. L. Skov, *J. Mater. Chem. C* **2019**, *8*, 1273.
- [34] G. Landi, A. Sorrentino, S. Iannace, H. C. Neitzert, *Nanotechnology* **2017**, *28*, 054005.
- [35] Z. Wang, D. Tonderys, S. E. Leggett, E. K. Williams, M. T. Kiani, R. S. Steinberg, Y. Qiu, I. Y. Wong, R. H. Hurt, *Carbon* **2016**, *97*, 14.
- [36] J. Modolo, Y. Denoyer, F. Wendling, P. Benquet, *Curr. Opin. Biomed. Eng.* **2018**, *8*, 38.
- [37] E. C. Salas, Z. Sun, A. Lüttge, J. M. Tour, *ACS Nano* **2010**, *4*, 4852.
- [38] G. Lalwani, W. Xing, B. Sitharaman, *J. Mater. Chem. B Mater. Biol. Med.* **2014**, *2*, 6354.
- [39] H. Bai, W. Jiang, G. P. Kotchey, W. A. Saidi, B. J. Bythell, J. M. Jarvis, A. G. Marshall, R. A. S. Robinson, A. Star, *J. Phys. Chem. C, Nanomater. Interfaces* **2014**, *118*, 10519.
- [40] R. Kurapati, J. Russier, M. A. Squillaci, E. Treossi, C. Ménard-Moyon, A. E. D. Rio-Castillo, E. Vazquez, P. Samorì, V. Palermo, A. Bianco, *Small* **2015**, *11*, 3985.
- [41] M. Chen, X. Qin, G. Zeng, *Trends Biotechnol.* **2017**, *35*, 836.
- [42] C. Zhu, L. Liu, M. Fan, L. Liu, B. Dai, J. Yang, D. Sun, *RSC Adv.* **2014**, *4*, 55044.
- [43] L. Liu, C. Zhu, M. Fan, C. Chen, Y. Huang, Q. Hao, J. Yang, H. Wang, D. Sun, *Nanoscale* **2015**, *7*, 13619.
- [44] M. Irimia-Vladu, *Chem. Soc. Rev.* **2014**, *43*, 588.
- [45] K. O. Siegenthaler, A. Künkel, G. Skupin, M. Yamamoto, in *Synthetic Biodegradable Polymers* (Eds: B. Rieger, A. Kunkel, G. W. Coates, R. Reichardt, E. Dinjus, T. Zevaco), Springer, Berlin **2011**.
- [46] W. Zhou, T. Xiong, C. Shi, J. Zhou, K. Zhou, N. Zhu, L. Li, Z. Tang, S. Chen, *Angew. Chem. Int. Ed.* **2016**, *55*, 8416.
- [47] C. Shi, N. Zhu, N. Kang, P. Wu, X. Zhang, Y. Zhang, *Biotechnol. Prog.* **2017**, *33*, 1314.
- [48] P.-K. Yang, Z.-H. Lin, K. C. Pradel, L. Lin, X. Li, X. Wen, J.-H. He, Z. L. Wang, *ACS Nano* **2015**, *9*, 901.
- [49] D. Shakhiviel, A. S. Dahiya, R. Mukherjee, R. Dahiya, *Curr. Opin. Chem. Eng.* **2021**, *34*, 100753.
- [50] M. Chakraborty, J. Kettle, R. Dahiya, *IEEE J. Flex. Electron.* **2022**, *1*, 4.
- [51] W. Ruppen, S. Derry, H. J. McQuay, R. A. Moore, *BMC Palliat. Care* **2007**, *6*, 3.
- [52] A. Quaille, *Int. Orthopaed.* **2012**, *36*, 451.
- [53] S. Tirakunwichcha, W. Tulvatana, K. Kulvichit, *Am J Ophthalmol.* **2003**, *136*, 944.
- [54] M. A. Kafi, A. Paul, A. Vilouras, R. Dahiya, *Biosens. Bioelectron.* **2020**, *147*, 111781.
- [55] M. A. Kafi, A. Paul, A. Vilouras, E. S. Hosseini, R. S. Dahiya, *IEEE Sens. J.* **2020**, *20*, 6794.
- [56] M. Bhattacharjee, A. Vilouras, R. S. Dahiya, *IEEE Sens. J.* **2020**, *20*, 7494.
- [57] M. Bhattacharjee, S. Middya, P. Escobedo, J. Chaudhuri, D. Bandyopadhyay, R. Dahiya, *Biosens. Bioelectron.* **2020**, *165*, 112333.
- [58] M. E. V. Zapata, C. D. G. Tovar, J. H. M. Hernandez, *Biomolecules* **2020**, *10*, 1616.
- [59] H. Bao, Y. Pan, Y. Ping, N. G. Sahoo, T. Wu, L. Li, J. Li, L. H. Gan, *Small* **2011**, *7*, 1569.
- [60] Y. Qu, J. Wang, Q. Ma, W. Shen, X. Pei, S. You, Q. Yin, X. Li, *Water Res.* **2018**, *143*, 260.
- [61] M. Dvorak, W. Oswald, Z. Wu, *Sci. Rep.* **2013**, *3*, 2289.
- [62] S. Sahu, G. C. Rout, *Int. Nano Lett.* **2017**, *7*, 81.
- [63] N. Richter, Z. Chen, A. Tries, T. Prechtel, A. Narita, K. Müllen, K. Asadi, M. Bonn, M. Kläui, *Sci. Rep.* **2020**, *10*, 1988.
- [64] M. B. Lerner, N. Kybert, R. Mendoza, R. Villechenon, M. A. B. Lopez, A. T. C. Johnson, *Appl. Phys. Lett.* **2013**, *102*, 183113.

- [65] J. Son, S. Lee, S. J. Kim, B. C. Park, H.-K. Lee, S. Kim, J. H. Kim, B. H. Hong, J. Hong, *Nat Comm.* **2016**, *7*, 13261.
- [66] F. Liu, W. T. Navaraj, N. Yogeswaran, D. H. Gregory, R. Dahiya, *ACS Nano* **2019**, *13*, 3257.
- [67] T. T. Cui, J. C. Li, W. Gao, Q. Jiang, *Phys. Chem. Chem. Phys.* **2018**, *20*, 2230.
- [68] J. Zhao, C. He, R. Yang, Z. Shi, M. Cheng, W. Yang, G. Xie, D. Wang, D. Shi, G. Zhang, *Appl. Phys. Lett.* **2012**, *101*, 063112.
- [69] P. Pillai, M. M. De Souza, V. K. Tewary, Y. Zhang, in *Modeling, Characterization, And Production Of Nanomaterials*, Woodhead Publishing, Swaston, Cambridge **2015**, pp. 203–231.
- [70] G.-X. Ni, Y. Zheng, S. Bae, H. R. Kim, A. Pachoud, Y. S. Kim, C.-L. Tan, D. Im, J.-H. Ahn, B. H. Hong, B. Özyilmaz, *ACS Nano* **2012**, *6*, 1158.
- [71] S. Deng, V. Berry, *Mater. Today* **2016**, *19*, 197.
- [72] W. Zhu, T. Low, V. Perebeinos, A. A. Bol, Y. Zhu, H. Yan, J. Tersoff, P. Avouris, *Nano Lett.* **2012**, *12*, 3431.
- [73] E. C-D. Río, P. Mallet, H. González-Herrero, J. L. Lado, J. Fernández-Rossier, J. M. Gómez-Rodríguez, J.-Y. Veillen, I. Brihuega, *Adv. Mater.* **2020**, *32*, 2001119.
- [74] G. Dobrik, P. Nemes-Incze, B. Majérus, P. Süle, P. Vancsó, G. Piszter, M. Menyhárd, B. Kalas, P. Petrik, L. Henrard, L. Tapasztó, *Nat. Nanotechnol.* **2022**, *17*, 61.
- [75] Z. Dai, Z. Gao, S. S. Pershoguba, N. Tiwale, A. Subramanian, Q. Zhang, C. Eads, S. A. Tenney, R. M. Osgood, C.-Y. Nam, J. Zang, A. T. C. Johnson, J. T. Sadowski, *Phys. Rev. Lett.* **2021**, *127*, 086805.
- [76] X. Li, R. Zhang, W. Yu, K. Wang, J. Wei, D. Wu, A. Cao, Z. Li, Y. Cheng, Q. Zheng, R. S. Ruoff, H. Zhu, *Sci. Rep.* **2012**, *2*, 1.
- [77] K. Li, W. Yang, M. Yi, Z. Shen, *Smart Mater. Struct.* **2021**, *30*, 085027.
- [78] C. Lou, S. Wang, T. Liang, C. Pang, L. Huang, M. Run, X. Liu, *Materials* **2017**, *10*, 1068.
- [79] M. J. Christoe, J. Han, K. Kalantar-Zadeh, *Adv. Mater. Technol.* **2020**, *5*, 1900733.